Plasmon-plasmon interactions supported by a one-dimensional plasmonic crystal: Rabi phase and generalized Rabi frequency

Zhengchen Liang,[1,*] Longyu Qing,[1,*] Zhoujun Li,[1] Xuan Trung Nguyen,[2] Ting Xu,[3] Antonietta De Sio,[2] Hong Zhang,[1,4] Christoph Lienau,[2] and Wei Wang[1,†]

[1]*College of Physics, Sichuan University, Chengdu 610064, China*

[2]*Carl von Ossietzky Universität, Institut für Physik, Oldenburg 26129, Germany*

[3]*National Laboratory of Solid State Microstructures, College of Engineering and Applied Sciences and Collaborative Innovation Center of Advanced Microstructures, Nanjing University, Nanjing 210093, China*

[4]*Key Laboratory of High Energy Density Physics and Technology of Ministry of Education, Sichuan University, Chengdu 610065, China*

(Received 16 April 2020; revised 3 June 2020; accepted 30 June 2020; published 15 July 2020)

Plasmon-plasmon interactions are key in controlling light at the nanoscale and in the development of high-performance plasmonic devices. Sophisticated design and efficient dynamic control of such devices requires a precise description of both spectral responses and ultrafast temporal dynamics in plasmon-plasmon coupling systems. Here, a microscopic model based on the Heisenberg-Langevin formalism is developed for generic plasmon-plasmon interacting systems. The validity of the model was experimentally supported by precisely reproducing the output spectra of interacting plasmons in a one-dimensional plasmonic crystal. We discussed the inheritance from an initial phase to the Rabi phase, which is accompanied by the vacuum fluctuations dephasing the incoherent coupling channel. We further derived the generalized Rabi frequency between two coupled plasmonic modes. We demonstrate that the interplay between the Rabi phase and the coupling-induced incoherent damping process modulates the ultrafast dynamics of the polariton modes, resulting in distinctly different spectral responses including the degeneracy and reversing in the polariton branches. Our model can be readily extended to any other bosonic coupling systems such as interacting nanoparticles and photonic/plasmonic cavities, thus holding great promise and potential applications in nanocircuits and cavity QED.

DOI: 10.1103/PhysRevB.102.035422

I. INTRODUCTION

With their ability to confine light at subwavelength scale by excitation of surface plasmons (SPs), metallic nanostructures play a significant role in a broad range of applications in nanoscience [1]. In metal-based plasmonic nanostructures, particularly with strongly coupled elementary components, coupling of SPs may lead to many optical effects that dominate their optical properties such as shifts or splittings of plasmon frequencies [2,3], occurrence of Fano-type spectral responses [4–6], and modified radiance property of plasmonic modes [6–9]. Different methods including classical electromagnetic theory, Mie scattering theory, and semiclassical approach have been developed for modeling plasmon-plasmon interactions in a variety of plasmonic nanostructures [10–13]. It is worth mentioning that an analytical theory of plasmon hybridization method has been widely used to provide a simple and intuitive picture of coupled SPs in complex nanostructures [14]. Using the method of mode regulation, coherent coupling effects such as Fano-shaped plasmon resonances and sub/superradiance can be explained by treating interacting SPs classically in plasmonic systems [15,16].

In applications of active plasmonics, dynamic control and manipulation of plasmons in high-performance nanodevices requires a deep understanding of microscopic coupling dynamics including ultrafast coherent energy exchange and coupling-induced incoherent damping mechanisms in the interacting plasmons [17], for which a microscopic description is highly desired. So far, only a few studies focus on real-time plasmon-plasmon coupling characteristics and the resulting optical responses with an existing complex coupling coeffcient [18]. An eligible microscopic model for plasmon-plasmon coupling to describe both spectral responses and the ultrafast coupling dynamics under the interplay between an initial phase difference and the coherent/incoherent channels still need to be developed.

In this paper, we develop a microscopic model to provide a clear picture of plasmonic interactions based on the widely applied Heisenberg-Langevin formalism [19–22]. A gold nanoslit array fabricated on a glass substrate was employed as a test platform to verify the validity of our model. In this system, we can not only precisely extract linear spectral characteristics including dispersion, spectral widths, and the spectral amplitude of the interacting SPs as bosonic polariton modes [23], but we also have full access to the ultrafast response in temporal properties including the coherent and incoherent coupling dynamics, as well as the evolutions of polariton populations. We derive the correct

*These authors contributed equally to this work.
†w.wang@scu.edu.cn

 ©2020 American Physical Society

form of the non-Hermitian total Hamiltonian with an existing Rabi phase, and analytically perform the exact definition of the generalized Rabi frequency, which governs the coherent interactions between two coupled plasmonic modes under large detunings. We also demonstrate the exact role of the Rabi phase [24] and coupling-induced incoherent damping process [25] in modulating the population dynamics of the polariton modes and the resultant spectral responses. Our microscopic model can be readily applied to describe other bosonic coupling systems such as interacting nanoparticles and photonic/plasmonic cavities, providing a viable route for studying nanocircuits or cavity-QED systems.

II. RESULTS

A. Heisenberg-Langevin formalism for bosonic interacting system

To describe plasmon-plasmon interactions in the microscopic regime, let us consider an interacting system with quantized plasmonic modes labeled by $l = 1, \ldots, n$ at resonance frequencies ω_l. The free Hamiltonian $H_{\rm F}$ can be presented in number state representation by the bosonic creation (annihilation) operators $\hat{a}_l^\dagger$ ($\hat{a}_l$) as $H_{\rm F} = \sum_l \hbar\omega_l(\hat{a}_l^\dagger\hat{a}_l + 1/2)$. Their coherent interactions, under the rotating-wave approximation (RWA), is presented as $H_{\rm I} = \sum_{k<l}\hbar(g_{kl}\hat{a}_k^\dagger\hat{a}_l + {\rm H.c.})$, with g_{kl} being the coherent coupling strength. Driven by an incident harmonic field with frequency ω, the driving Hamiltonian reads [26] $H_{\rm D} = i\hbar(\sum_l \sqrt{\Gamma_l}A_l e^{-i\omega t}\hat{a}_l^\dagger) + {\rm H.c.}$, with Γ_l and A_l being the total decay rates of polariton modes and the coupling coefficients to the incidence, respectively. Of importance are the radiation and dissipation processes of the plasmons to the continuum reservoir, given by $H_{\rm R} = \int \hbar\omega'(\hat{b}_{\omega'}^\dagger\hat{b}_{\omega'} + \hat{c}_{\omega'}^\dagger\hat{c}_{\omega'})d\omega'$, which leads to the Hamiltonian of system-reservoir interaction $H_{\rm S} = i\hbar\int(\sum_l B_l\hat{b}_{\omega'}^\dagger\hat{a}_l + C_l\hat{c}_{\omega'}^\dagger\hat{a}_l)d\omega' + {\rm H.c.}$ The bosonic $\hat{b}_{\omega'}$ with coupling coefficient B_l presents the continuum radiative modes, and $\hat{c}_{\omega'}$ presents the continuum phononic background leading to Ohmic loss. Hence, the total Hamiltonian reads $H = H_{\rm F} + H_{\rm I} + H_{\rm D} + H_{\rm R} + H_{\rm S}$. The time evolution of any operator $\hat{O}$ describing a physically observable property of the system follows the Heisenberg equation of motion $\dot{\hat{O}} = (i/\hbar)[H, \hat{O}]$, which gives rise to

$$\begin{aligned}
\dot{\hat{a}}_l &= -i\omega_l\hat{a}_l - i\sum_{k<l} g_{kl}^*\hat{a}_k - i\sum_{k>l} g_{lk}\hat{a}_k + \sqrt{\Gamma_l}A_l e^{-i\omega t} \\
&\quad - B_l\int b_{\omega'}d\omega' - C_l\int c_{\omega'}d\omega', \\
\dot{\hat{b}}_{\omega'} &= -i\omega' b_{\omega'} + \sum_{l=1}^{n} B_l\hat{a}_l, \\
\dot{\hat{c}}_{\omega'} &= -i\omega' c_{\omega'} + \sum_{l=1}^{n} C_l\hat{a}_l,
\end{aligned} \tag{1}$$

in which B_l and C_l are the radiative and the dissipative coupling coefficients between subsystems $\hat{a}_l$ and the continuum reservoir, respectively. Following the convention, in the time domain we integrate

$$\begin{aligned}
\hat{b}_{\omega'}(t) &= b_{\omega'}(0)e^{-i\omega' t} + \int_0^t \sum_{l=1}^{n} B_l\hat{a}_l e^{-i\omega'(t-t')}dt', \\
\hat{c}_{\omega'}(t) &= c_{\omega'}(0)e^{-i\omega' t} + \int_0^t \sum_{l=1}^{n} C_l\hat{a}_l e^{-i\omega'(t-t')}dt'
\end{aligned} \tag{2}$$

to receive

$$\begin{aligned}
\dot{\hat{a}}_l &= -i\omega_l\hat{a}_l - i\sum_{k<l} g_{kl}^*\hat{a}_k - i\sum_{k>l} g_{lk}\hat{a}_k + \sqrt{\Gamma_l}A_l e^{-i\omega t} \\
&\quad -\pi\sum_{k=1}^{n}(B_kB_l + C_kC_l)\hat{a}_k + \hat{F}_l,
\end{aligned} \tag{3}$$

where the operator of random fluctuations $\hat{F}_l$ satisfies the Markoff condition $\langle\hat{F}_l^\dagger(t)\hat{F}_l(t')\rangle = \delta(t-t')$. Microscopically, the direct impact of vacuum fluctuations on the populations of plasmonic modes are small enough, but we shall pay attention to its phase effect in the following sections. Note that the incoherent coupling coefficient γ_{kl} is introduced to characterize the coupling-induced incoherent damping channel [25] between individual plasmonic modes via the continuum reservoir [18,27,28]. In terms of

$$\begin{aligned}
\Gamma_l &= \Gamma_{l,{\rm r}} + \Gamma_{l,{\rm nr}} = 2\pi B_l^2 + 2\pi C_l^2 \equiv 2\gamma_l, \\
\Gamma_{kl} &= 2\pi(B_kB_l + C_kC_l) \equiv 2\gamma_{kl}
\end{aligned} \tag{4}$$

with the total decay rate $\Gamma_l = 2\gamma_l$ of an individual polariton mode ω_l, we plug Eq. (4) back into Eq. (3) where the detuning $\Delta_l = \omega_l - \omega$ emerges. The Heisenberg-Langevin equations of the entire system under RWA are derived as

$$\begin{aligned}
\dot{\hat{a}}_l &= -i\sum_{k>l}(g_{lk} - i\gamma_{lk})\hat{a}_k - i\sum_{k<l}(g_{kl}^* - i\gamma_{kl})\hat{a}_k \\
&\quad - \left(i\Delta_l + \frac{1}{2}\Gamma_l\right)\hat{a}_l + \sqrt{\Gamma_l}A_l + \hat{F}_l.
\end{aligned} \tag{5}$$

Based on Eq. (5), the steady-state solutions and the real-time dynamics of the plasmonic interacting system can be readily obtained.

B. Plasmon-plasmon interactions supported by 1D narrow nanoslit array

To demonstrate the validity of our microscopic model, we have designed and fabricated a one-dimensional (1D) plasmonic nanoslit array, which is a widely applied platform [18,27] for plasmon excitations due to its capability of simultaneously supporting different plasmon modes with highly distinguishable dispersions that can be easily evaluated and tuned by the period of the nanoslit. The simple structural configuration and the ease of fabrication make it an ideal candidate for the study of plasmon-plasmon interactions.

The shallow nanoslit array as a platform for plasmon-plasmon interactions is fabricated with the focused ion beam milling technique. As depicted in Fig. 1(a), it is prepared on a 30-nm-thick gold film deposited on a Ti-coated (3 nm) SiO_2 substrate, with a period of $p = 680$ nm [see scanning electron microscope (SEM) image]. SPs are excited at both the air-metal (AM) and the substrate-metal (SM) interfaces

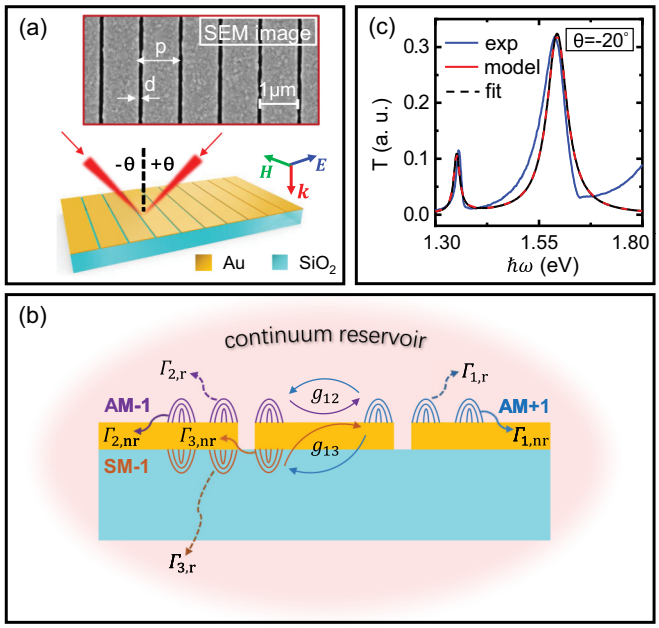

FIG. 1. (a) Schematic and SEM image (inset) of the gold nanoslit array deposited on a SiO_2 substrate. (b) A diagram describing coherent interactions characterized by coupling constant g_{12} and g_{13}, respectively, as well as damping pathways of SP modes AM[+1], AM[−1], and SM[−1] with labels $l = 1, 2, 3$ representing their radiative decay $\Gamma_{l,\mathrm{r}}$ and nonradiative decay $\Gamma_{l,\mathrm{nr}}$. (c) Transmission spectrum (blue), together with the model result (red), and its Lorentzian-shaped fitting (dashed) at incident angle $\theta = 20°$.

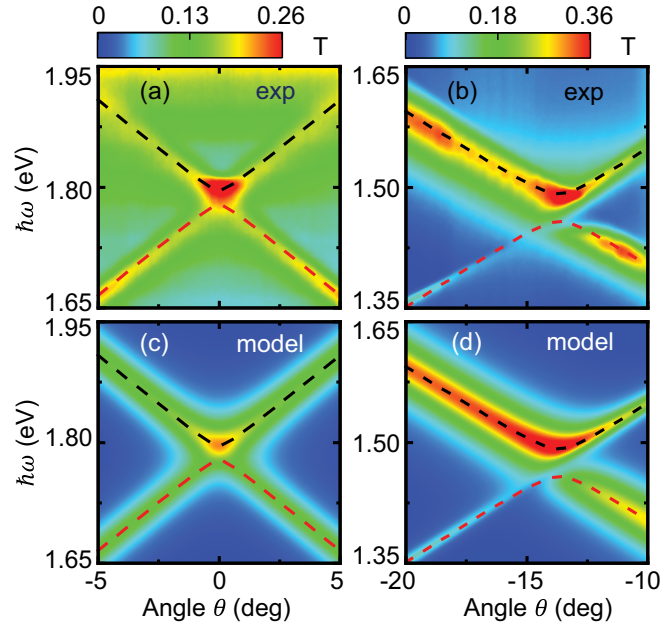

FIG. 2. Measured (a),(b) and calculated (c),(d) angle-resolved transmission spectra (in color scale) showing the AM-AM (a),(c) and AM-SM (b),(d) couplings, respectively. The dashed lines give the modeled polariton dispersion.

by grating coupling, which transfers an additional momentum $\Delta k = m(2\pi/p)$ (with m being an integer) to the incident photons. Importantly, the SPs are also featured by their tunable resonances due to the in-plane momentum $k_{x,\mathrm{SP}} = k_0 \sin\theta \pm \Delta k$, which is dependent on the incident angle θ. Figure 1(c) depicts the transmission spectrum (blue) measured at an incident angle $\theta = 20°$ where two strong resonances appear: one at ∼1.35 eV with Lorentzian line shape and the other at ∼1.6 eV with a sightly Fano-shaped peak, corresponding to SP modes AM[$m = +1$] and SM[$m = -1$], respectively. The transmission spectrum essentially arises from two interfering channels, i.e., the reemitted resonant SPs and the nonresonant, direct transmission through the nanoslit array [18]. The narrow and shallow slit array configuration was chosen here to minimize the phase difference between the two pathways, so that their interference leads to Lorentzian-shaped transmission spectra instead of complicated Fano line shapes. Besides, at large incidence angle the slightly Fano-shaped SM[−1] mode actually results from its interference with the SM[+2] mode at higher energy (see Fig. 7 in Appendix A).

We perform angle-resolved linear transmission measurements on the nanoslit array by varying θ with an angular resolution of 0.1° (see Appendix A for the details of the experimental setup). The measured angle-resolved transmission spectra in Figs. 2(a) and 2(b) clearly map the SP band structures with three well-distinguished branches. Symmetric AM[±1] branches overlap at a resonance energy of ∼1.79 eV at normal incidence, whereas asymmetric AM[+1] and SM[−1] branches are in resonance at lower energy (∼1.47 eV) with an apparent splitting [Fig. 2(b)]. These observed spectral features indicate plasmon-plasmon interactions among different modes, which can be quantitatively described by our microscopic model. In such nanoslit array, different damping pathways coexist, as depicted in Fig. 1(b). The decay rates of the individual plasmon modes $\Gamma_l = \Gamma_{l,\mathrm{r}} + \Gamma_{l,\mathrm{nr}}$ are primarily dominated by radiative damping $\Gamma_{l,\mathrm{r}}$. Here, $l = 1, 2, 3$ denote AM[+1], AM[−1], and SM[−1], respectively. We consider the contribution of the nonradiative damping as $\hbar\Gamma_{l,\mathrm{nr}} = 5$ meV for all modes [18]. Considering the influence of frequency-dependent Rayleigh scattering on the radiative damping and the small angular ranges studied in our experiment, the radiative damping $\hbar\Gamma_{1(2),\mathrm{r}} = 45$ meV for the angular range of $-5° \leqslant \theta \leqslant 5°$, and $\hbar\Gamma_{1,\mathrm{r}} = 13$ meV, $\hbar\Gamma_{3,\mathrm{r}} = 54$ meV for $-20° \leqslant \theta \leqslant -10°$ are optimized in our model as constant values.

With an optimal set of coherent and incoherent coupling strengths $\hbar g_{12} = 10$ meV, $\hbar\gamma_{12} = 1.8$ meV, $\hbar g_{13} = 20$ meV, and $\hbar\gamma_{13} = 1.7$ meV, the measured angle-resolved transmission spectra are very nicely reproduced with the radiative output power $\Phi_{\mathrm{rad}} = \sum_{l=1}^{3} \Gamma_{l,\mathrm{r}} \langle \hat{a}_l^\dagger \hat{a}_l \rangle$ retrieved from either the steady-state solution [29] or equivalently the time-domain convergent solution of Eq. (5) (see Appendix B). Note that the observed AM-AM and AM-SM interactions are in the intermediate coupling regime [30], which are classified under the criterion $|\Gamma_k - \Gamma_l|/4 < g_{kl} < \sqrt{(\Gamma_k^2 + \Gamma_l^2)}/8$.

C. Sub- and superradiant polariton modes

Based on the quantitative description of the static optical response in Figs. 2(c) and 2(d), the spectral characteristics can be extracted with high precision by fitting the calculated spectra to a Lorentzian line shape $T(\omega) = |t(\omega)|^2$ by [31,32]

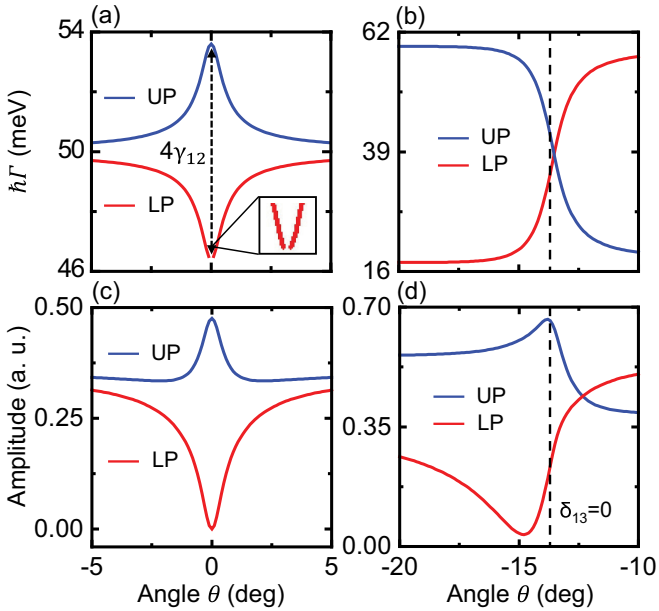

FIG. 3. Spectral widths of upper polariton (UP) and lower polariton (LP) branches retrieved from the model solution and fitted by a Lorentzian line shape for (a) AM-AM coupling and (b) AM-SM coupling. UP and LP amplitudes retrieved from the model solution and fitted by a Lorentzian line shape for (c) AM-AM coupling and (d) AM-SM coupling.

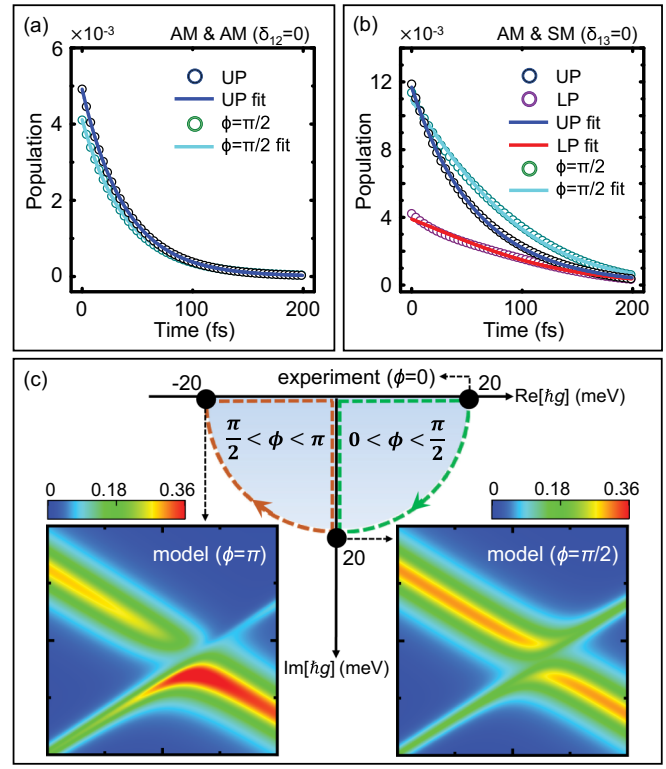

FIG. 4. The calculated (circles) and fitted (solid lines) total population(s) of hybrid mode(s) at zero detuning $\delta_{kl} = \omega_k - \omega_l = 0$ for (a) AM-AM coupling and (b) AM-SM coupling with Rabi phase $\phi = \pi/2$. (c) The angle-resolved transmission spectra derived from our model with a Rabi phase $\phi = \pi$ (left) and $\phi = \pi/2$ (right) for AM-SM coupling.

$t(\omega) = \sum_{j=+,-}[b_j\gamma_j e^{i\phi_j}/(\omega - \omega_j + i\gamma_j)]$ with the spectral amplitudes b_l. Calculated eigenenergies of the hybrid modes, the dashed lines in Fig. 2, nicely match to the resonances both in the measured and the calculated angle-resolved transmission maps. The accuracy of our approach in modeling of the static response of the hybrid system can be confirmed by the good matching of the modeled spectrum (solid red) to the measured result (solid blue) in Fig. 1(c).

The spectral widths ($\hbar\Gamma_\pm$) and the amplitudes are also extracted and are shown in Figs. 3(a)–3(d), respectively. For the symmetric AM-AM coupling, as AM[±1] modes are brought closer to resonance, the full-width at half-maximum (FWHM) of UP/LP branch increases/decreases, resulting in a super-/subradiant UP/LP mode due to the presence of coupling-induced incoherent interaction [18,27,28]. This is accompanied by a drastic increase/decrease in the transmission amplitudes of the UP/LP branch, as shown in Fig. 3(c). Particularly, the amplitude of LP vanishes at zero detuning $\theta = 0°$, and the FWHM of LP becomes undefined [inset of Fig. 3(a)]. This vanishing polariton resonance is essentially the direct consequence of the degeneracy of AM[±1] modes at normal incidence: AM[±1] modes become undistinguishable and the coupling process between these two identical modes gives rise to a pure single "bright" UP mode and a completely "dark" LP mode. Importantly, the degeneracy of plasmons at this critical point eliminates the physical meaning of the cross-damping term γ_{12}, which transferred directly to the damping of the degenerated mode, leading to a single broadened Lorentzian-type UP resonance. This is readily confirmed by the real-time dynamics at UP resonance. As shown in Fig. 4(a), the population evolving in time (blue circles) derived from our model experiences an ultrafast decrease from its steady state. This can be perfectly fitted to an exponentially decaying function, indicating a freely damped UP excitation at zero detuning.

This phenomenon occurs only for symmetric AM-AM coupling at the degeneracy point. As for AM-SM coupling, the two asymmetric SP modes, induced at different interfaces, possess distinct intrinsic damping properties and oscillator strength, which result in sub- and superradiant hybrid states with their width difference governed again by the cross-damping term $4\gamma_{13}$ at zero detuning ($\theta = -13.7°$). As clearly shown in Fig. 3(b), this aspect is further supported by the enhanced/suppressed decay rate of UP/LP total population in the time domain. From a maximum likelihood estimation by the criterion $\dot{N} = -\alpha N - \beta N^2$, the curves best fit the parameter $\beta > 0$ at the UP resonance, and $\beta < 0$ at the LP resonance, as plotted in Fig. 4(b). Moreover, a dramatically reduced amplitude and a narrowing of the linewidth of the LP mode at larger incidence angles $\theta < -14°$ were observed due to the asymmetry coupling of AM[+1] and SM[−1], resulting in a much darker (not totally dark) LP branch with respect to a bright UP branch.

D. From an initial phase difference between coupling modes to the Rabi phase

Apart from the success in microscopically explaining the coupling-induced damping mechanism for sub-/superradiant

polaritons, our microscopic model also interprets the microscopic origin of the Rabi phase, which appears as a phase factor in the complex coupling constant $g = |g|e^{i\phi}$. Essentially, the Rabi phase ϕ is believed to be relevant to the spatial distance and the resultant relative phase difference between the two individual subsystems [24]. In our previous work, the coupling constants with negative values have been observed in plasmonic systems coupled to organic/inorganic semiconductors [27,33,34], or to monolayer two-dimensional atomic crystals [28,35]. In this sense, the negative g corresponds to Rabi phase $\phi = \pi$. In the present nanoslit array, the coherent coupling constants are found to be real positive values for both AM-AM and AM-SM couplings, corresponding to Rabi phase $\phi = 0$.

Based on the microscopic model, we then further reveal that the Rabi phase originates from the initial phase difference between two individual modes which cannot be eliminated by a U(1) gauge transform. In the dynamics (5), this phase difference is absorbed in the coherent coupling term via H_{I}, resulting in the complex g. Moreover, in the system-reservoir interaction, the residual factor of phase difference is eliminated by continuum integrals in frequency domain [Eq. (1)]. Hence the Rabi phase which modulates the coherent coupling rate g, has completely no impact on the incoherent coupling regime.

Importantly, for seeking the correct form of incoherent behavior in the total steady-state Hamiltonian (B5), we have to consider the presence of an initial phase difference that generates the Rabi phase. In the two-mode coupling case, which may be experimentally realized by driving the two plasmonic modes by external fields A_1 and A_2 with a phase difference $e^{i\phi}$, we can add the phase factor to $a_2 \mapsto a_2 e^{i\phi}$ appearing in the two-mode version of (5). Supposing that the time-domain integration (2) still classically preserves the initial phase, the dynamics may appear differently for $k, l = 1, 2$:

$$\dot{\hat{a}}_l = -i\sum_{k>l}(g_{lk} - i\gamma_{lk})\hat{a}_k - i\sum_{k<l}(g_{kl}^* - i\gamma_{kl}^*)\hat{a}_k - \left(i\Delta_l + \frac{1}{2}\Gamma_l\right)\hat{a}_l + \sqrt{\Gamma_l}A_l, \tag{6}$$

in which we have absorbed the phase factor into γ_{12} in the same way for g_{12} as

$$\dot{\hat{a}}_1 = -\left(i\Delta_1 + \frac{\Gamma_1}{2}\right)\hat{a}_1 + \sqrt{\Gamma_1}A_1 - (i\underbrace{g_{12}e^{i\phi}}_{g_{12}} - \underbrace{\gamma_{12}e^{i\phi}}_{\gamma_{12}})\hat{a}_2,$$

$$\dot{\hat{a}}_2 = -\left(i\Delta_2 + \frac{\Gamma_2}{2}\right)\hat{a}_2 + \sqrt{\Gamma_2}A_2 - (i\underbrace{g_{12}e^{-i\phi}}_{g_{12}^*} - \underbrace{\gamma_{12}e^{-i\phi}}_{\gamma_{12}^*})\hat{a}_1 \tag{7}$$

assuming (2) has preserved the phase factor. Note that in the classical framework, equivalent dynamics of (6) can be derived, as discussed in the literature [36,37]. However, this is not the case in the presence of vacuum fluctuation [24,34]. In the Heisenberg-Langevin Eq. (3), the fluctuation operators $\hat{F}_l$ under the Markoff condition are originated from the same time-domain integration as (2) in the incoherent coupling channel, which result in purely dephasing real coupling coefficients γ_{kl}. An existing initial phase difference between coupling plasmonic modes is erased by the dephasing in the incoherent channel through the integral (2). Therefore, the correct form of the total Hamiltonian (B5) adopted in our previous work [27,34] and the dynamics (5) in our current microscopic model is different from (6) because of the vacuum fluctuations in the incoherent channel of system-reservoir interaction. This fact indicates that the Rabi phase is the only inheritance from a coherent phase difference between the coupling modes, while the dephasing effect of vacuum fluctuation presents in the incoherent coupling channel, despite its small direct impact on the populations of plasmonic modes in the microscopic regime.

The Rabi phase, originating from the initial U(1) phase difference between the two individual modes, can modulate the output spectra and the ultrafast dynamics. Figures 4(a) and 4(b) demonstrate the effect of the Rabi phase on both AM-AM and AM-SM coupling at zero detuning. At $\phi = \pi/2$, the calculated UP/LP populations experience exactly the same decay curve (green circles) under equal initial eigenvalue. The output spectral response in Fig. 4(c) (right) then shows a symmetric branch of equal amplitude in the transmission spectra at zero detuning, which differs from the measured spectra ($\phi = 0$) with much brighter/darker UP/LP branches [Fig. 2(b)]. As ϕ increases from $\pi/2$ to π, the reversed UP/LP population dynamics further modulated the reversed configuration of spectral amplitudes in Fig. 4(c) (left). The Rabi phase is thus responsible for the observed phenomena [16] of the reversed optical responses of the hybrid modes.

Knowing that an initial phase difference absorbed in the Hamiltonian H_{I} originates a nonzero Rabi phase, we further investigate the exact role of the Rabi phase interplaying with the incoherent coupling channel γ_{kl}, which results in the non-Hermitian total Hamiltonian [see Eq. (B5) in Appendix B], in modulating the ultrafast dynamics of plasmon-plasmon coupling. For interacting plasmonic modes $a_k(t)$ and $a_l(t)$, we address $a_k = p_{kl}a_l$ with p_{kl} the complex ratio of modal coefficients satisfying $N_k/N_l = |p_{kl}|^2$. Back to Eq. (5), it appears

$$\dot{p}_{kl} = i(g_{kl}^* - i\gamma_{kl})p_{kl}^2 + \left[i\delta_{lk} + \tfrac{1}{2}(\Gamma_l - \Gamma_k)\right]p_{kl} - i(g_{kl} - i\gamma_{kl}) \tag{8}$$

with the detuning $\delta_{kl} = \omega_k - \omega_l$. Its discriminant $\Delta_{kl} = [i\delta_{lk} + (\Gamma_l - \Gamma_k)/2]^2 - 4\Lambda_{kl}$ with $\Lambda_{kl} = |g_{kl}|^2 - \gamma_{kl}^2 - 2i\gamma_{kl}\mathrm{Re}[g_{kl}]$, determines

$$\frac{p_{kl} - p_{kl,+}}{p_{kl} - p_{kl,-}} = C_{kl}\exp(\sqrt{\Delta_{kl}}t), \tag{9}$$

the analytic curve system of the solution $p_{kl}(t)$ with a complex constant C_{kl}, where $p_{kl,\pm}$ are the roots of Eq. (C3) under $\dot{p}_{kl} = 0$. We can then recognize the *generalized Rabi frequency* f_{kl} as the imaginary part of the exponent, i.e., $f_{kl} = \mathrm{Im}[\sqrt{\Delta_{kl}}]$, which characterizes the periodicity in the evolving fraction of populations in plasmon-plasmon coupling. More details on the analytical derivation of the generalized Rabi frequency is given in Appendix C.

Figures 5(a)–5(d) plot the fractions of populations N_1/N_2 (in logarithm scale) in UP and LP hybrid modes of coupling between AM[+1] and AM[−1] SP modes for varying Rabi

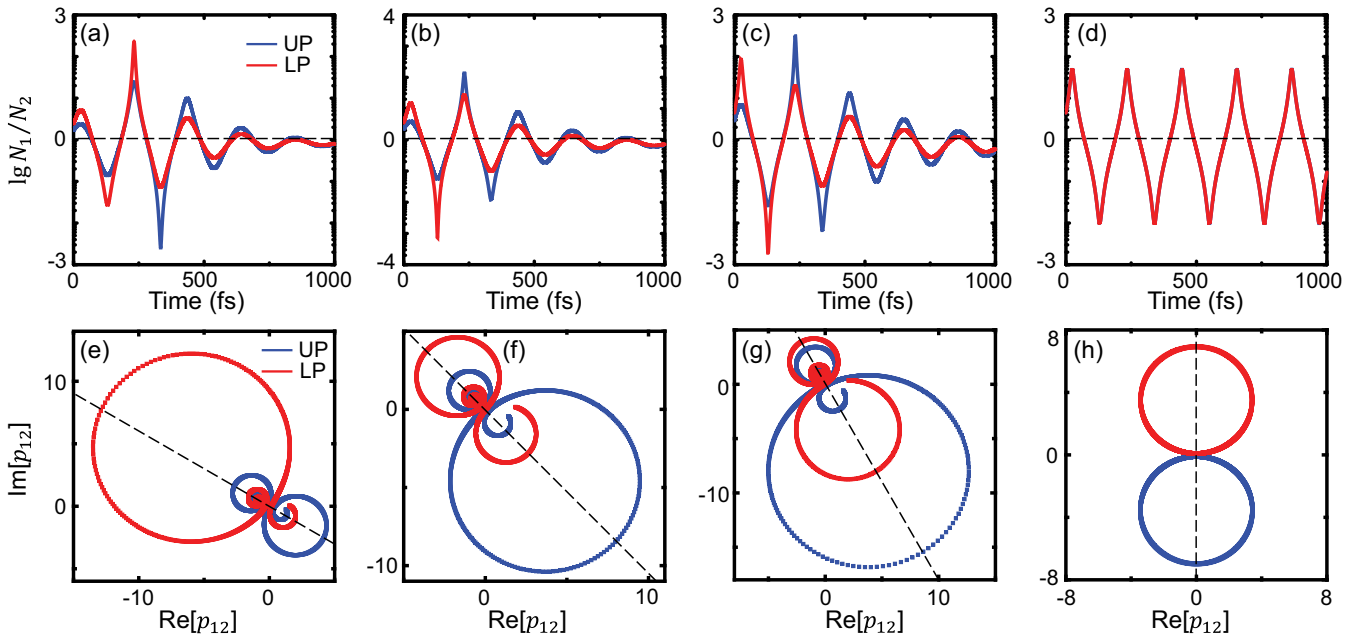

FIG. 5. The fractions of populations N_1/N_2 (in logarithmic scale) in UP and LP hybrid modes of coupling between AM[+1] and AM[−1] SP modes at zero detuning $\delta_{12} = 0$ and $\hbar\gamma_{12} = 1.8$ meV. The ultrafast dynamics is modulated by the Rabi phase (a) $\phi = 30°$, (b) $\phi = 45°$, (c) $\phi = 60°$, and (b) $\phi = 90°$. (e)–(h) The corresponding trajectory to (a)–(d) of $p_{12}(t)$ on its complex plane within 1000 fs. The dashed lines link the two convergence points on the complex plane at time $t \to \pm\infty$ of the solved analytic curve system, which vary under different Rabi phases.

phase at zero detuning ($\delta_{12} = 0$) for $\hbar\gamma_{12} = 1.8$ meV. Apparently, the fractions of AM[±1] populations in the hybrid modes experience ultrafast oscillations with a fixed period of 207 fs, i.e., the Rabi period, corresponding to the coherent coupling energy $2\hbar|g_{12}| = 20$ meV. In this sense, the generalized Rabi frequency f_{kl} returns to the Rabi frequency at zero detuning. The coherent population transfer between the plasmon modes can also be intuitively visualized by plotting modal coefficients p_{kl} in a complex plane, as shown in Figs. 5(e)–5(h). Here, a population transfer period is clearly identified as a complete circle in the complex plane.

The interplay between a nonzero Rabi phase and the incoherent channel γ_{kl} leads to distinct behavior of population dynamics of the interacting plasmons, which can be readily analyzed based on the plots in the complex plane. Note that with this γ_{kl}, the total Hamiltonian [method Eq. (B5)] is equivalent to the construction from the density-matrix formalism with a Lindblad form introduced in [34]. For the cases with the Rabi phase of $\phi = 30°$, 45°, and 60°, the fractions of population N_1/N_2 finally converge to finite values after an infinite long relaxation time, as shown in Figs. 5(e)–5(g). Whereas, for $\phi = 90°$, the fraction does not converge, exhibiting two infinite circles for both UP and LP modes with the persistence of time-translation symmetry.

To look into this fact, we focus on the universal constraints Eq. (4) on the cross-damping γ_{kl} by the total dampings γ_k and γ_l of the individual modes, which have also been established in light-matter interacting systems [35]. In our case, the constraints can already be interpreted as [25] $\gamma_{12} = \sqrt{\gamma_1\gamma_2}(\boldsymbol{\mu}_1 \cdot \boldsymbol{\mu}_2)$ where $\boldsymbol{\mu}_{1,2}$ denotes the dipole moment of AM[±1]. According to our derivation, the Rabi phase $\phi = \pi/2$ indicates the phase difference between individual AM[±1] oscillations of $\pi/2$ under the U(1) phase symmetry. Therefore, in all periods of the individual dipole oscillation T_1, the orthogonality of $\int_0^{T_1} \sin(2\pi t/T_1)\cos(2\pi t/T_1)dt = 0$ cancels the time-averaged population exchange via the incoherent channel, which holds only for $\phi = \pi/2$. Indeed, when the Rabi phase is nonzero, the incoherent damping term $\gamma_{12} = 1.8$ meV breaks the time-translation symmetry of AM[±1] population fractions [Figs. 5(a)–5(c)]. If the two plasmon modes only coherently interact in absence of the incoherent damping pathway ($\gamma_{12} = 0$), the time-translation symmetry of AM[±1] population fractions in UP and LP branches will always hold regardless of the Rabi phase, as shown in Fig. 6. It is worth mentioning that the incoherent channel does affect the total decay of AM[±1] populations, as comparing Figs. 5(d) and 5(h) with Figs. 6(d) and 6(h) where the fraction of population N_1/N_2 appears slightly different. Moreover, a complex g_{12} (nonzero Rabi phase) indicates distinguishable AM[±1] even at zero detuning, unlike the situation in Fig. 3(a), which leads to nondegenerate UP and LP hybrid modes that are again modulated by γ_{12}.

Therefore, the population dynamics in the hybrid polariton modes and the output spectral response can be efficiently modulated by cooperatively controlling the Rabi phase and the incoherent damping term. One possible way of achieving the desired Rabi phase is to carefully adjust the spatial distance (probably in subwavelength scale) between the interfaces at which plasmons with different modes are excited. While for the incoherent coupling term, it can be tuned by tailoring the dipolar orientations of the individual plasmons. This is of particular use for the design of sophisticated metallic nanostructures for active plasmonic devices.

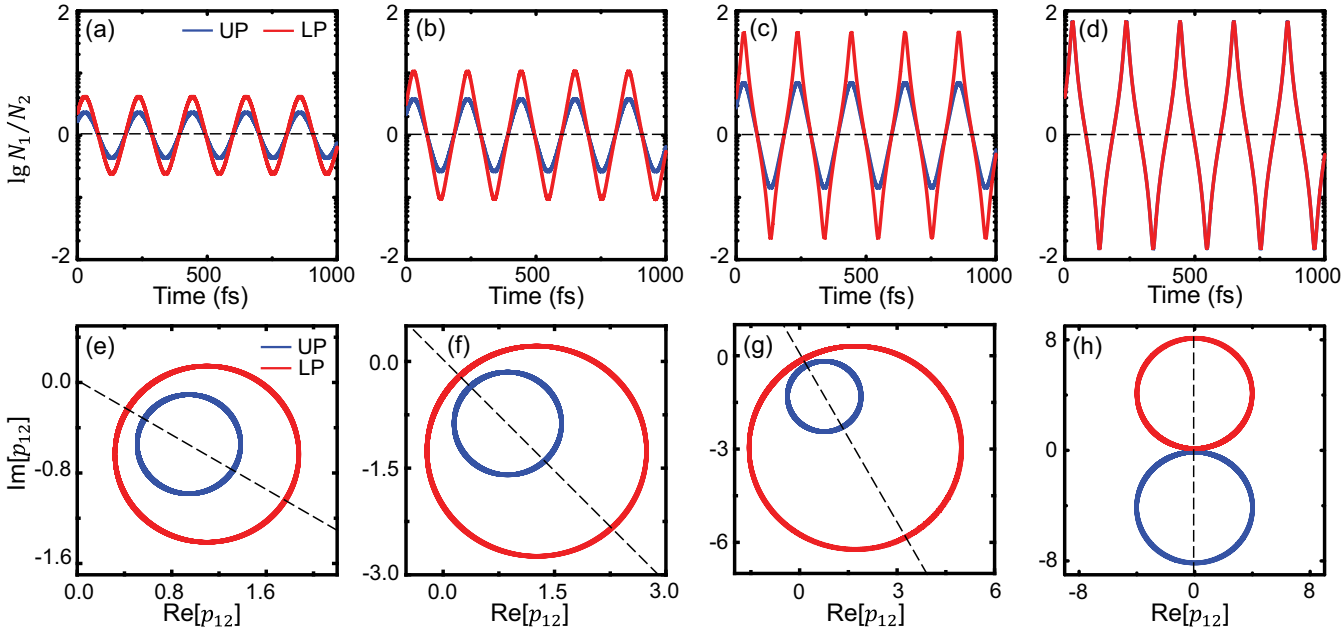

FIG. 6. The fractions of populations N_1/N_2 (in logarithmic scale) in UP and LP hybrid modes of coupling between AM[+1] and AM[−1] SP modes at zero detuning $\delta_{12} = 0$ and $\hbar\gamma_{12} = 0$. The ultrafast dynamics is modulated by the Rabi phase (a) $\phi = 30°$, (b) $\phi = 45°$, (c) $\phi = 60°$, and (b) $\phi = 90°$. (e)–(h) The corresponding trajectory to (a)–(d) of $p_{12}(t)$ on its complex plane within 1000 fs.

III. CONCLUSION

We have developed a microscopic model for bosonic interacting systems, providing microscopic pictures and details of spectral responses and the ultrafast dynamics of interacting plasmons. The model is experimentally set up and tested by reproducing the measured angle-resolved transmission spectra of a narrow nanoslit array which supports SPs on AM and SM interfaces. Within this approach, we are able to precisely extract both the linear spectral characteristics and the temporal coupling dynamics of the interacting systems. Moreover, we discussed the microscopic origin of the Rabi phase and the total Hamiltonian, from which we analytically derived the exact definition of the generalized Rabi frequency. We also performed the essential role of the Rabi phase and the coupling-induced incoherent damping in modulating the population dynamics of the polariton modes and the resultant spectral responses. This method for analyzing the pure bosonic systems with its flexibility and generality, may have promising applications in the interacting systems including photonic/plasmonic cavities.

ACKNOWLEDGMENTS

This work is supported by the National Natural Science Foundation of China (Grants No. 11974254, No. 61675139, and No. 11974253), the National Key R&D Program of China (2017YFA0303600), and the Innovation Program of Sichuan University (Grant No. 2018SCUH0074).

APPENDIX A: ANGLE-RESOLVED TRANSMISSION SPECTROSCOPY

In our spectroscopic measurement, the sample was fixed vertically on a sample holder which is mounted on an electrically driven high-precision rotation stage. A home-built microscope is equipped in set up to monitor the location of the beam spot on the sample. Under the illumination of a broadband (1.1 eV–2 eV) white light laser source (Fianium SC-450-4) with a repetition rate of 80 MHz, transmission spectra were recorded by varying the angle of incidence θ ranging from $-30°$ to $-10°$ with a small step size of 0.1°.

In the present nanoslit array prepared on glass substrate, there are two interfaces that can support SP excitations: AM and SM interfaces, as shown in Fig. 7 (left). Consider the AM interface as an example; SP can be excited by compensating the momentum mismatch between the in-plane wave vector of SP $k_{x,\mathrm{SP}}$ and the incoming far-field radiation $k_{x,0}$ in the $+x$ direction. The periodic grating provides an additional reciprocal vector Δk, in such a way that the momentum mismatch between the far-field radiation and the SPP dispersion relation is compensated: $k_{x,\mathrm{SP}} = k_{x,0} \pm m\Delta k = k_0 \sin\theta \pm m(2\pi/p)$. Here, k_0 is the wave vector of the incoming far-field radiation in free space. Solutions of $k_{x,\mathrm{SP}}$ are possible for different integer m at each angle of incidence θ.

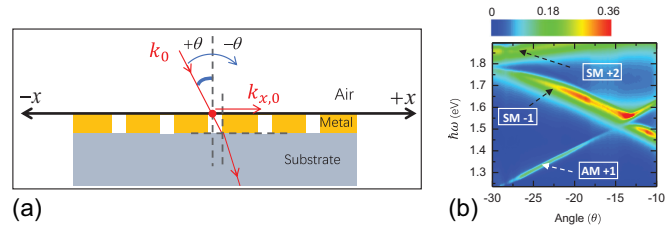

FIG. 7. (a) Schematic of SP excitations in nanoslit array on glass substrate (i.e., the grating configuration [38]), and (b) angle-resolved transmission spectrum (in color scale) measured on the gold nanoslit array with period of $p = 680$ nm.

As shown in Fig. 7 (right), we can clearly see three SP branches, which are identified as AM[+1], SM[−1] and SM[+2], respectively. Note that at larger angle of incidence part of the SM[−1] branch approaches the SM[+2] branch, and their interference leads to Fano-shaped transmission spectra, as shown in Fig. 1(c) in the main text. Therefore, we only discussed the AM-SM coupling in the range of $-20^\circ \leqslant \theta \leqslant -10^\circ$ where the influence of the SM[+2] branch can be neglected.

APPENDIX B: EIGENFUNCTION AND STEADY-STATE SOLUTION

Considering the coupling between two plasmonic modes, the Heisenberg-Langevin equation reads explicitly

$$\dot{\hat{a}}_1 = -i(g_{12} - i\gamma_{12})\hat{a}_2 - \left(i\Delta_1 + \tfrac{1}{2}\Gamma_1\right)\hat{a}_1 + \sqrt{\Gamma_1}A_1 + \hat{F}_1, \tag{B1}$$

$$\dot{\hat{a}}_2 = -i(g_{12}^* - i\gamma_{12})\hat{a}_1 - \left(i\Delta_2 + \tfrac{1}{2}\Gamma_2\right)\hat{a}_2 + \sqrt{\Gamma_2}A_2 + \hat{F}_2. \tag{B2}$$

By setting $\dot{\hat{a}}_l = 0$ a steady-state solution appears as

$$\hat{a}_1 = [\sqrt{\Gamma_1}A_1(i\Delta_2 + \Gamma_2/2) - i(g_{12} - i\gamma_{12})\sqrt{\Gamma_2}A_2]/\beta, \tag{B3}$$

$$\hat{a}_2 = [\sqrt{\Gamma_2}A_2(i\Delta_1 + \Gamma_1/2) - i(g_{12}^* - i\gamma_{12})\sqrt{\Gamma_1}A_1]/\beta, \tag{B4}$$

where $\beta = (i\Delta_1 + \Gamma_1/2)(i\Delta_2 + \Gamma_2/2) + (g_{12} - i\gamma_{12})(g_{12}^* - i\gamma_{12})$ is the determinant of coupling between two bosonic modes. This steady-state solution corresponds to the Hamiltonian in the quantum jump approach

$$H = (\hat{a}_1^\dagger \quad \hat{a}_2^\dagger)\begin{pmatrix} \omega_1 - i\frac{\Gamma_1}{2} & g_{12} - i\gamma_{12} \\ g_{12}^* - i\gamma_{12} & \omega_2 - i\frac{\Gamma_2}{2} \end{pmatrix}\begin{pmatrix} \hat{a}_1 \\ \hat{a}_2 \end{pmatrix} \tag{B5}$$

for the plasmon-plasmon interaction. By diagonalizing Eq. (B5), the steady-state solutions are reproduced from the eigenfunction in the quantum jump approach.

APPENDIX C: DETAILS IN THE CALCULATION FOR PLASMON-PLASMON COUPLING

In the general case of plasmon-plasmon coupling, i.e., with a nonzero Rabi phase [39], we continue with the ratio of modal coefficients $p_{kl}(t) = a_k(t)/a_l(t)$, where $a_k(t)$ and $a_l(t)$ are the evolving modal coefficients as observables in an interaction picture under the number state representation. From the equation of motion for plasmon-plasmon interaction, we obtain

$$a_l\dot{p}_{kl} + p_{kl}\dot{a}_l = -i(g_{kl} - i\gamma_{kl})a_l - \left(i\Delta_k + \tfrac{1}{2}\Gamma_k\right)p_{kl}a_l, \tag{C1}$$

$$\dot{a}_l = -i(g_{kl}^* - i\gamma_{kl})p_{kl}a_l - \left(i\Delta_l + \tfrac{1}{2}\Gamma_l\right)a_l \tag{C2}$$

when removing the driving field and omitting the noises. Plugging Eq. (C2) into Eq. (C1) we have the modal coefficient a_l canceled which leads to the ordinary differential equation (ODE)

$$\dot{p}_{kl} = i(g_{kl}^* - i\gamma_{kl})p_{kl}^2 + \left[i\delta_{lk} + \tfrac{1}{2}(\Gamma_l - \Gamma_k)\right]p_{kl} - i(g_{kl} - i\gamma_{kl}) \tag{C3}$$

governing the complex ratio $p_{12}(t)$, where $\delta_{kl} = \omega_k - \omega_l$ is the detuning between two individual modes and $\delta_{lk} = -\delta_{kl}$. Denoting

$$\begin{aligned} A &= i(g_{kl}^* - i\gamma_{kl}), \\ B &= i\delta_{lk} + \tfrac{1}{2}(\Gamma_l - \Gamma_k), \\ C &= -i(g_{kl} - i\gamma_{kl}) \end{aligned} \tag{C4}$$

to express the discriminant

$$\Delta_{kl} = B^2 - 4AC = \left[i\delta_{lk} + \tfrac{1}{2}(\Gamma_l - \Gamma_k)\right]^2 - 4\Lambda_{kl} \tag{C5}$$

which controls the ODE, Eq. (C3), in complex domain we have

$$\frac{1}{p_{kl,+} - p_{kl,-}}\int\left(\frac{1}{p_{kl} - p_{kl,+}} - \frac{1}{p_{kl} - p_{kl,-}}\right)dp_{kl} = At, \tag{C6}$$

where $p_{kl,\pm}$ are the roots of Eq. (C3) under the condition of $\dot{p}_{kl} = 0$. Integrate

$$\ln\frac{p_{kl} - p_{kl,+}}{p_{kl} - p_{kl,-}} = (p_{kl,+} - p_{kl,-})At \cdot K \tag{C7}$$

and take the exponent; absorbing a complex constant into $K = \ln C_{kl}$ we receive

$$\begin{aligned} \frac{p_{kl} - p_{kl,+}}{p_{kl} - p_{kl,-}} &= C_{kl}\exp\left[i(g_{kl}^* - i\gamma_{kl})(p_{kl,+} - p_{kl,-})t\right] \\ &= C_{kl}\exp\left(\sqrt{\Delta_{kl}}\,t\right) \end{aligned} \tag{C8}$$

as the analytic solution $p_{kl}(t)$ of the governing equation, Eq. (C3). Since the periodicity in $p_{kl}(t)$ is determined by the imaginary part of the exponent, the generalized Rabi frequency appears $f_{kl} = \mathrm{Im}[i(g_{kl}^* - i\gamma_{kl})(p_{kl,+} - p_{kl,-})] = \mathrm{Im}[\sqrt{\Delta_{kl}}]$.

[1] W. L. Barnes, A. Dereux, and T. W. Ebbesen, Nature (London) **424**, 824 (2003).

[2] E. Prodan and P. Nordlander, Nano Lett. **3**, 543 (2003).

[3] M. Kim, H. Kwon, S. Lee, and S. Yoon, ACS Nano **13**, 12100 (2019).

[4] W. J. Padilla, A. J. Taylor, C. Highstrete, M. Lee, and R. D. Averitt, Phys. Rev. Lett. **96**, 107401 (2006).

[5] I. M. Pryce, K. Aydin, Y. A. Kelaita, R. M. Briggs, and H. A. Atwater, Nano Lett. **10**, 4222 (2010).

[6] S. R. K. Rodriguez, A. Abass, B. Maes, O. T. A. Janssen, G. Vecchi, and J. Gómez Rivas, Phys. Rev. X **1**, 021019 (2011).

[7] F. Hao, E. M. Larsson, T. A. Ali, D. S. Sutherland, and P. Nordlander, Chem. Phys. Lett. **458**, 262 (2008).

[8] M. Fleischhauer and M. D. Lukin, Phys. Rev. Lett. **84**, 5094 (2000).
[9] B. Gallinet, T. Siegfried, H. Sigg, P. Nordlander, and O. J. Martin, Nano Lett. **13**, 497 (2013).
[10] T. W. Preist, N. P. K. Cotter, and J. R. Sambles, J. Opt. Soc. Am. A **12**, 1740 (1995).
[11] W. L. Barnes, T. W. Preist, S. C. Kitson, and J. R. Sambles, Phys. Rev. B **54**, 6227 (1996).
[12] D. Sarkar and N. J. Halas, Phys. Rev. E **56**, 1102 (1997).
[13] Y. A. Akimov and H. S. Chu, Nanotechnology **23**, 444004 (2012).
[14] E. Prodan, C. Radloff, N. J. Halas, and P. Nordlander, Science **302**, 419 (2003).
[15] K. G. Lee and Q.-H. Park, Phys. Rev. Lett. **95**, 103902 (2005).
[16] J. E. Kihm, Y. C. Yoon, D. J. Park, Y. H. Ahn, C. Ropers, C. Lienau, J. Kim, Q. H. Park, and D. S. Kim, Phys. Rev. B **75**, 035414 (2007).
[17] L. Martin-Moreno, F. J. Garcia-Vidal, H. J. Lezec, K. M. Pellerin, T. Thio, J. B. Pendry, and T. W. Ebbesen, Phys. Rev. Lett. **86**, 1114 (2001).
[18] C. Ropers, D. J. Park, G. Stibenz, G. Steinmeyer, J. Kim, D. S. Kim, and C. Lienau, Phys. Rev. Lett. **94**, 113901 (2005).
[19] N. Thakkar, C. Cherqui, and D. J. Masiello, ACS Photonics **2**, 157 (2015).
[20] S. J. Whalen and H. J. Carmichael, Phys. Rev. A **93**, 063820 (2016).
[21] D. Boyanovsky and D. Jasnow, Phys. Rev. A **96**, 062108 (2017).
[22] A. Asghari Nejad, H. R. Askari, and H. R. Baghshahi, Appl. Opt. **56**, 2816 (2017).
[23] D. Xu, X. Xiong, L. Wu, X.-F. Ren, C. E. Png, G.-C. Guo, Q. Gong, and Y.-F. Xiao, Adv. Opt. Photonics **10**, 703 (2018).
[24] R. Pomraenke, Optical excitations in novel nanostructures: Single-walled carbon nanotubes and metal-semiconductor-hybrids, Ph.D. thesis, Carl von Ossietzky Universität Oldenburg, 2014.
[25] U. Akram, Z. Ficek, and S. Swain, Phys. Rev. A **62**, 013413 (2000).
[26] C. Savage and H. Carmichael, IEEE J. Quantum Electron. **24**, 1495 (1988).
[27] W. Wang, P. Vasa, R. Pomraenke, R. Vogelgesang, A. De Sio, E. Sommer, M. Maiuri, C. Manzoni, G. Cerullo, and C. Lienau, ACS Nano **8**, 1056 (2014).
[28] S. Zhang, H. Zhang, T. Xu, W. Wang, Y. Zhu, D. Li, Z. Zhang, J. Yi, and W. Wang, Phys. Rev. B **97**, 235401 (2018).
[29] P. Peng, Y. C. Liu, D. Xu, Q. T. Cao, G. Lu, Q. Gong, and Y. F. Xiao, Phys. Rev. Lett. **119**, 233901 (2017).
[30] W. Liu, Y. Wang, C. H. Naylor, B. Lee, B. Zheng, G. Liu, A. T. C. Johnson, A. Pan, and R. Agarwal, ACS Photonics **5**, 192 (2018).
[31] Y. Li, A. Chernikov, X. Zhang, A. Rigosi, H. M. Hill, A. M. van der Zande, D. A. Chenet, E.-M. Shih, J. Hone, and T. F. Heinz, Phys. Rev. B **90**, 205422 (2014).
[32] A. E. Miroshnichenko, S. Flach, and Y. S. Kivshar, Rev. Mod. Phys. **82**, 2257 (2010).
[33] P. Vasa, R. Pomraenke, S. Schwieger, Y. I. Mazur, V. Kunets, P. Srinivasan, E. Johnson, J. E. Kihm, D. S. Kim E. Runge, G. Salamo, and C. Lienau, Phys. Rev. Lett. **101**, 116801 (2008).
[34] P. Vasa, W. Wang, R. Pomraenke, M. Lammers, M. Maiuri, C. Manzoni, G. Cerullo, and C. Lienau, Nat. Photonics **7**, 128 (2013).
[35] P. Xie, Z. Liang, Z. Li, W. Wang, W. Wang, T. Xu, X. Kuang, L. Qing, D. Li, and J. Yi, Phys. Rev. B **101**, 045403 (2020).
[36] R. Taubert, M. Hentschel, and H. Giessen, J. Opt. Soc. Am. B **30**, 3123 (2013).
[37] M. Frimmer and L. Novotny, Am. J. Phys. **82**, 947 (2014).
[38] H. Raether, Springer Tracts Mod. Phys. **111**, 1 (1988).
[39] G. S. Agarwal, in *Quantum Optics*, edited by G. Höhler (Springer, Berlin, Heidelberg, 1974), pp. 1–128.